RESEARCH ARTICLE
doi: 10.2306/scienceasia1513-1874.2021.074

ScienceAsia 47 (2021): **585–593**

Synthesis and characterization of low-density porous $Ni_{0.55}Zn_{0.25}Cu_{0.20}Fe_2O_4$ (NZCFO) by sol-gel auto-combustion method

Qiushan Yu[a,b], **Yuchang Su**[a,*], **Rabigul Tursun**[a], **Zhongbao Luo**[a], **Jing Zhang**[a]

[a] School of Materials Science and Engineering, Central South University, Changsha 410083 China
[b] School of Physics and Optoelectronic Engineering, Yangtze University, Jingzhou 430023 China

*Corresponding author, e-mail: emlink@csu.edu.cn

Received 24 Jan 2021
Accepted 14 Jun 2021

ABSTRACT: Ni-Zn-Cu ferrite plays an important role in soft magnetic material applications due to its excellent magnetic properties, but its high bulk density hinders its practical use. Therefore, some low-density porous Ni-Zn-Cu ferrite powders were prepared by a sol-gel auto-combustion method using metal nitrates and citric acid as raw materials to solve the problem. The microstructure, morphology, magnetic properties, and microwave absorption performance of the ferrite were studied by TG-DSC, XRD, SEM, BET, FT-IR, VSM, and Vector Network Analyzer. The results revealed that the xerogels formed from nitrate and citric acid could undergo auto-combustion in air under the external conditions, and the release of heat and gas during the process can promote the formation of a multi-layered internal cavity structure in the ferrite to yield only a half bulk density of the general ferrite. The purity, morphology, grain size, and saturation magnetization of $Ni_{0.55}Zn_{0.25}Cu_{0.20}Fe_2O_4$ could be controlled by heat treatments at different temperatures and durations. The synthesized $Ni_{0.55}Zn_{0.25}Cu_{0.20}Fe_2O_4$ had excellent soft magnetic properties, low-density, and good microwave absorption properties, which make it an excellent microwave absorbing material with great promising practical application.

KEYWORDS: low-density, auto-combustion method, magnetic properties, mesoporous, microwave absorbers

INTRODUCTION

The rapid development of information technology in recent years has precipitated an ever-increasing abundance of electromagnetic signals in space, contributing to various sources of "electromagnetic pollution" to people's living environment [1]. A promising strategy to reduce electromagnetic pollution of human habitats is utilized by electromagnetic protection technology in building materials to reduce the electromagnetic impact. Ni-Zn-Cu ferrite ($Ni_xZn_{1-x-y}Cu_yFe_2O_4$, NZCFO) has become one of the leading materials used for soft magnetic and microwave absorbing applications due to its high saturation magnetization, high resistivity, low coercive force, low preparation cost, and good absorbing performance [2–11].

NZCFO could be synthesized by several methods, such as sol-gel method [2], laser deposition [3], co-precipitation [4, 5], auto-combustion [6], hydrothermal method [7], ball milling [8], precursor method [9], microemulsion technique [10], and ultrasonic cavitation [11]. As one of the most widely used building materials, sol gel had been prepared in combination with ferrite materials. The gel material exhibited good microwave absorbing properties and, consequently, effectively reduced pollution by electromagnetic waves. Therefore, this material enabled a simple and feasible method for protecting against electromagnetic pollution. Since the density of general ferrite of about 5.8 g/cm^3 is far exceeding the average density of composite materials, strategies toward reducing the problematically high density of ferrite materials focus primarily on combination and hollowing technologies. Ferrite and bamboo-charcoal were combined to effectively reduce bulk density and achieved good microwave absorption performance [12]. Nanoscale ferrite powder with a bulk density of only 4.03–4.32 g/cm^3 was produced using a hydrothermal template method with sulphates of nickel, zinc, and iron as raw materials, and triethylamine and polyethylene glycol as template [13]. A diatomite/nickel zinc ferrite composite was prepared by the sol-gel method, the density was reduced to 3.2–3.8 g/cm^3, and the dielectric and magnetic losses were higher than that

of general Ni-Zn ferrite within the 1–1000 MHz frequency band [14]. The citrate solution gel method was used to form strontium cobalt nickel barium ferrite composite powder which exhibited good microwave absorbing properties in the 5–8 GHz band on the surface of hollow beads [15]. However, these existing preparation methods had some disadvantages, such as fragile hollow templates, complex preparation processes, high preparation costs, and high density end products. In order to solve the shortcomings of the existing technologies, a method of xerogel formation using nitrate and citric acid as law materials could accomplish auto-combustion in air under the external conditions to obtain NZCFO. This method has the advantages of lower-density, simpler process, lower preparation cost, and better wave absorbing property of the product.

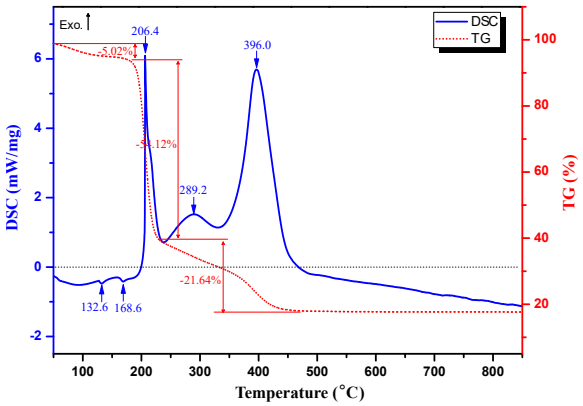

Fig. 1 TG-DSC curves of the xerogel.

MATERIALS AND METHODS

$Fe(NO_3)_3 \cdot 9\,H_2O$, $Ni(NO_3)_2 \cdot 6\,H_2O$, $Zn(NO_3)_2 \cdot 6\,H_2O$, and $Cu(NO_3)_2 \cdot 3\,H_2O$ were used as synthesis raw materials. Dilute $NH_3 \cdot H_2O$ served as a means of adjusting pH, while citric acid (CA) was used as chelating agent, NZCFO powder was prepared by the sol-gel auto-combustion method.

Typical preparation of NZCFO powder began with 0.1 mol $Fe(NO_3)_3 \cdot 9\,H_2O$, 0.0275 mol $Ni(NO_3)_2 \cdot 6\,H_2O$, 0.0125 mol $Zn(NO_3)_2 \cdot 6\,H_2O$, 0.01 mol $Cu(NO_3)_2 \cdot 3\,H_2O$, and 0.16 mol CA, which were each weighed, combined in 250 ml deionized water, and stirred until completely dissolved. During stirring, the pH value of the solution was adjusted to 7 via dropwise addition of dilute $NH_3 \cdot H_2O$ [16–21]. After 12 h continuous stirring, the solution was moved to a 120 °C blast drying oven and concentrated to form a brown xerogel which was ignited by external conditions and, therefore, underwent auto-combustion. After combustion, the resulting NZCFO, which exhibited fluffy dendrite morphology, was collected and subjected to heat treatment at various temperatures.

In order to test and characterize the sample's structure and properties, the thermogravimetric and differential scanning calorimetry (TG-DSC) analyses were carried out using a simultaneous thermal analyzer (STA449C, NETZSCH) from room temperature to 1000 °C at a heating rate of 10 °C/min in air. The crystalline phase of the powders was characterized using X-ray diffraction (XRD) at room temperature with a Rigaku D/Max 2500 powder diffractometer and Cu K_α radiation ($\lambda = 1.5406$ Å) at a scanning rate of 8°/min in the 2θ range of 10–70°. The sample structure bonding was characterized

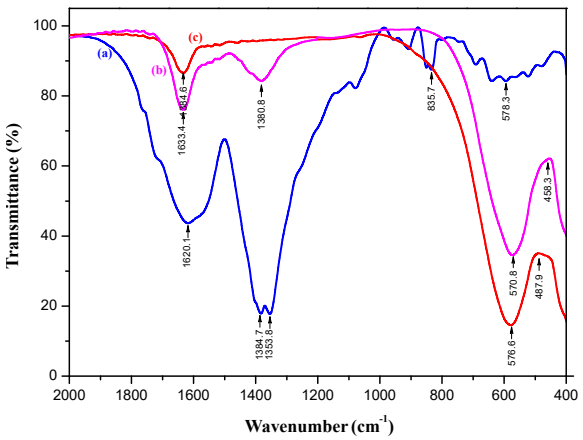

Fig. 2 IR spectra of: (a) xerogel before auto-combustion, (b) post auto-combustion xerogel, and (c) xerogel after auto-combustion and calcination at 600 °C for 4 h.

by Fourier-transform infrared (FT-IR) spectroscopy (Nicolet Nexus) over a range of 400–2000cm^{-1} and the magnetic properties of the NZCFO sample were characterized using a vibrating sample magnetometer (VSM, Lake Shore 7410) within 1T magnet at room temperature. Pycnometer method was used to acquisition the density of powders, Scanning electron microscopy (SEM, MIRA3 TESCAN) was used to obtain the morphology of the samples. Then, Surface area and porosity analyzer (Micromeritics, ASAP2460)was used to obtain the adsorption-desorption and the mesoporous distribution curves. The dielectric and magnetic losses of the sample were analyzed by Vector network analyzer (AV3672B-S).

Table 1 Density of xerogel powder after calcination at 600 °C for 4 h.

Measurement	Mass of m_1 (g)	Mass of m_2 (g)	Mass of m_3 (g)	Density ρ (g/cm^3)
1	0.1389	16.4664	16.5621	2.5105
2	0.2271	16.4639	16.6208	2.5259
3	0.1193	16.4656	16.5479	2.5175
Average	0.1618	16.4653	16.5769	2.5193

Table 2 Grain sizes and magnetic parameters (M_s, M_r, H_c and M_r/M_s) of NZCFO samples at room temperatures.

Sample	Grain size (nm)	M_s (emu/g)	M_r (emu/g)	H_c (Gauss)	M_r/M_s
NZCFO-NHT†	19.1 ± 0.3	45.72 ± 0.14	9.67 ± 0.17	101.92 ± 0.18	0.211
NZCFO-600	18.8 ± 0.3	61.49 ± 0.17*	13.38 ± 0.08	126.63 ± 0.27*	0.218
NZFCO-700	20.7 ± 0.5	64.29 ± 0.23	13.84 ± 0.09	91.08 ± 0.29	0.215
NZFCO-800	22.3 ± 0.4	67.13 ± 0.22	8.69 ± 0.08	49.44 ± 0.16	0.129

† No heat treatment.
* Reported by Gao: M_s = 36 emu/g and H_c = 167 Gauss [37].

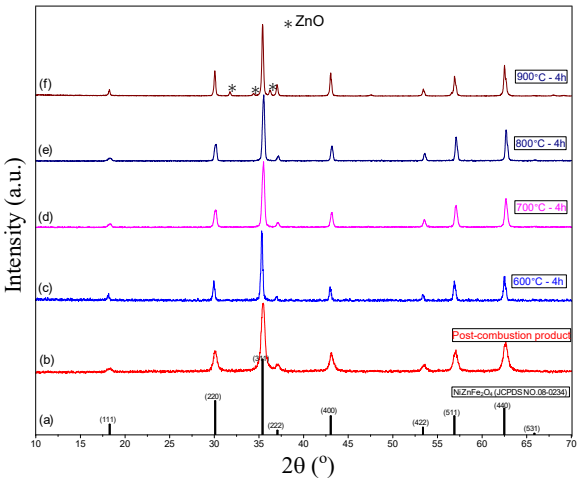

Fig. 3 The XRD patterns of: (a) $NiZnFe_2O_4$ standard and (b–f) $Ni_{0.55}Zn_{0.25}Cu_{0.20}Fe_2O_4$ calcinated at 600–900 °C in air.

RESULTS AND DISCUSSION

The prepared xerogel was analyzed by TG-DSC in air, and the obtained curves are shown in Fig. 1.

As the in air temperature increased from ambient to 200 °C, the sample existed in the endothermic state, with two weak peaks appearing near 132.6 °C and 168.6 °C indicating a combined mass loss of 5.35%. As shown in the FT-IR test curve (Fig. 2), the as-prepared xerogel (depicted by curve (a)) exhibited a strong water absorption characteristic peak near 1630 cm^{-1} that was significantly weakened after auto-combustion (curve (b)). Hence, it could be deduced that the sample underwent substantial water loss during the auto-combustion process. Therefore, the endothermic peak observed in this process between room temperature and 200 °C corresponds to the loss of CA hydrated water (Formula (1)) and the melting transformation of nitrate [22–24]. With further increasing temperature, the first exothermic peak formed near 206.4 °C and indicated a mass loss of about 54.12%. From the rate of mass loss, it could be inferred that the CA was oxidized by O_2 to generate exothermic reaction (Formula (2)) [24]. Near 289.2 °C, thermal decomposition mainly occurred according to Formula (3), following a relatively gentle process and, therefore, forming a relatively subdued second exothermic peak. Around 396.0 °C, the thermal decomposition mainly followed Formula (4), wherein the oxidation of nitrate occurred very rapidly, resulting in the formation of a steep third exothermic peak [22–25].

$$C_6H_8O_7 \cdot H_2O \rightarrow C_6H_8O_7 + H_2O - Q_{T1} \quad (1)$$

$$2\,C_6H_8O_7 + 9\,O_2 \rightarrow 12\,CO_2 + 8\,H_2O + Q_{T2} \quad (2)$$

$$NH_4NO_3 \rightarrow N_2O + 2\,H_2O + Q_{T3} \quad (3)$$

$$2\,NH_4NO_3 \rightarrow 2\,N_2 + O_2 + 2\,H_2O + Q_{T4} \quad (4)$$

Comparing the IR spectral curves of xerogel before (Fig. 2a) and after (Fig. 2b) auto-combustion revealed that the characteristic absorption peaks of nitrate and organic matter were rapidly weakened after combustion, indicating the involvement of these two substances in the reaction. In fact, Formula (4) indicated that the auto-combustion reaction was a thermally-induced redox reaction. The oxygen released from the redox reaction greatly increased the reaction rate, prompting the rapid release of a large amount of heat and gas from the melted xerogel and, thereby, promoting the reaction and

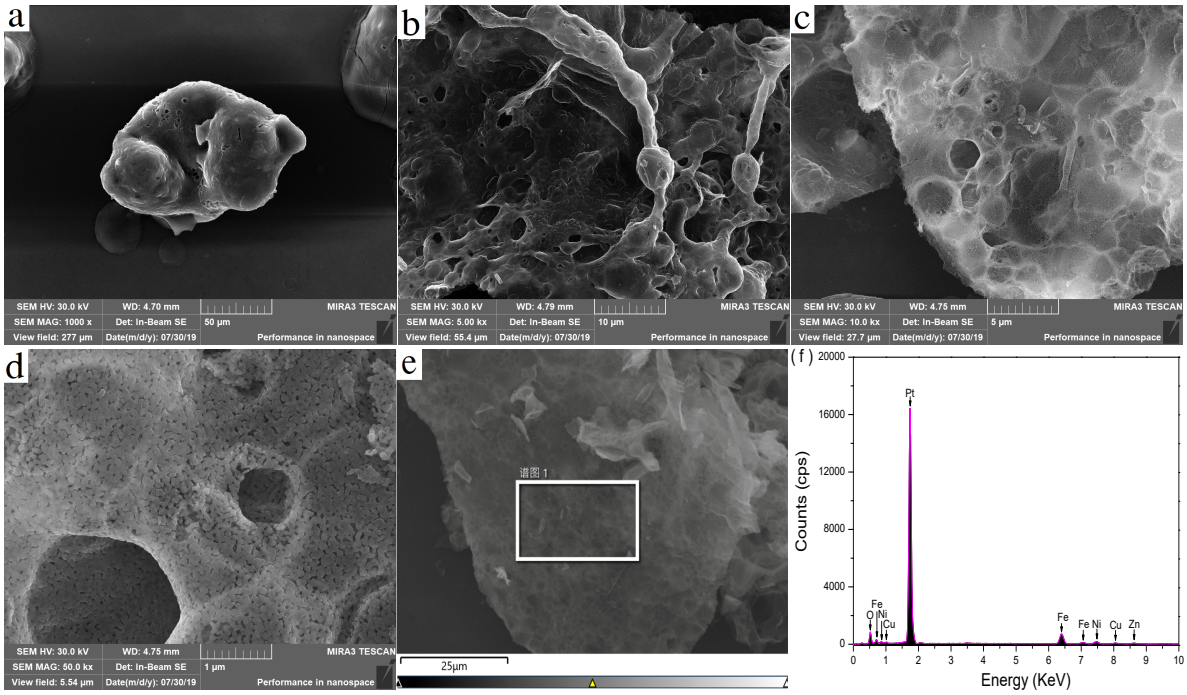

Fig. 4 SEM images of NZCFO: (a) xerogel morphology; (b) morphology of post auto-combustion xerogel; (c) low magnification; and (d) high magnification; (e) and (f) EDS spectrum of NZCFO.

organization of metal ions to form a loose nanopowder with spinel structure [26, 27].

An appropriate amount of xerogel sample, post auto-combustion sample, and calcinated sample each was mixed with KBr, and three mixtures were obtained and pressed into tablets. The tablets were measured across a wavenumber of 400–2000 cm^{-1} by FT-IR spectrometer. Curve (a) in Fig. 2, corresponding to the xerogel, exhibited a strong peak near 1630 cm^{-1} indicating water H—O—H bending vibration absorption, which was related to the crystal water of CA and adsorbed water of nitrate [28]. Near 1600 cm^{-1}, the characteristic absorption peak of citrate (antisymmetric stretching vibration band) indicated that CA formed a stable complex in the gel with metal cation. The CA salt exhibited characteristic vibration absorption bands near 1380 cm^{-1} and 830 cm^{-1}, while the characteristic absorption band of ferrite near 570 cm^{-1} was very weak, indicating that while the gel contained abundance of nitrate, the ferrite had not yet been formed in large quantities [28]. The curves corresponding to post auto-combustion samples in Fig. 2, namely curves (b) and (c), featured substantially weakened characteristic absorption peaks of water molecules near 1630 cm^{-1}, characteristic absorption peaks of citrate near 1600 cm^{-1}, and characteristic vibration absorption bands near 1380 cm^{-1} and 830 cm^{-1}. Furthermore, the 400–830 cm^{-1} region of curve (a) contained relatively modest features, while those of the post auto-combustion samples showed strong absorption bands at the ferrite characteristic peak near 570 cm^{-1}, indicating the involvement of both CA and nitrate ions in the processes of colloid formation and auto-combustion reaction, thereby contributing to the formation of ferrite. As such, these FT-IR spectra corroborated that the proposed Formulas (1)–(4) suitably described the auto-combustion process in the samples [28–31]. However, because the auto-combustion process always occurred in an unsealed container, the combustion reaction was incomplete, and traces of organic groups such as CA and residual nitrate ions remained in the sample. Nonetheless, high-temperature treatment elicited removal of these residues, so pure ferrite could be obtained (curve (c) in Fig. 2).

From Fig. 3, the XRD patterns of all samples contained the diffraction peaks of $NiZnFe_2O_4$ (JCPDS No.08-0234) with the spinel structure at 2θ diffraction angles of 18.3°, 30.1°, 35.4°, 37.1°, 43.0°, 53.4°, 56.9°, and 62.5° reflecting crystalline surfaces with (111), (220), (311), (222), (400), (422), (511), and (440), respectively. The absence

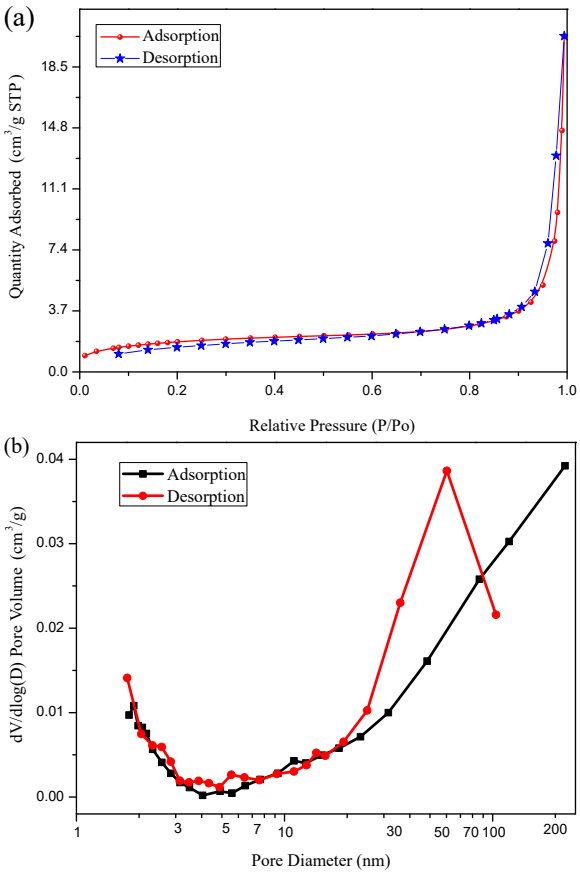

Fig. 5 Isothermal adsorption characteristics and pore size distribution characterization of NZCFO: (a) N_2 adsorption-desorption isotherm curves; (b) BJH pore size distribution curves.

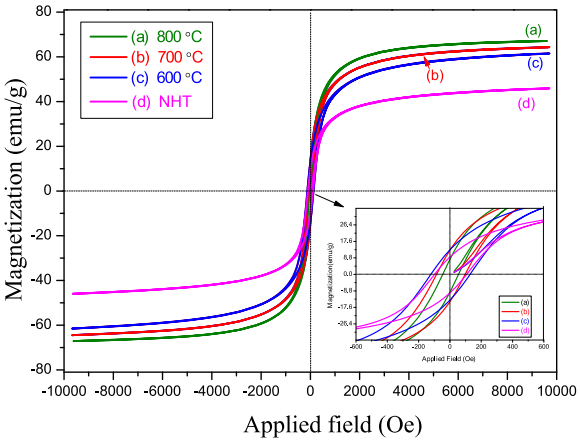

Fig. 6 M-H loops of NZCFO nanopowder.

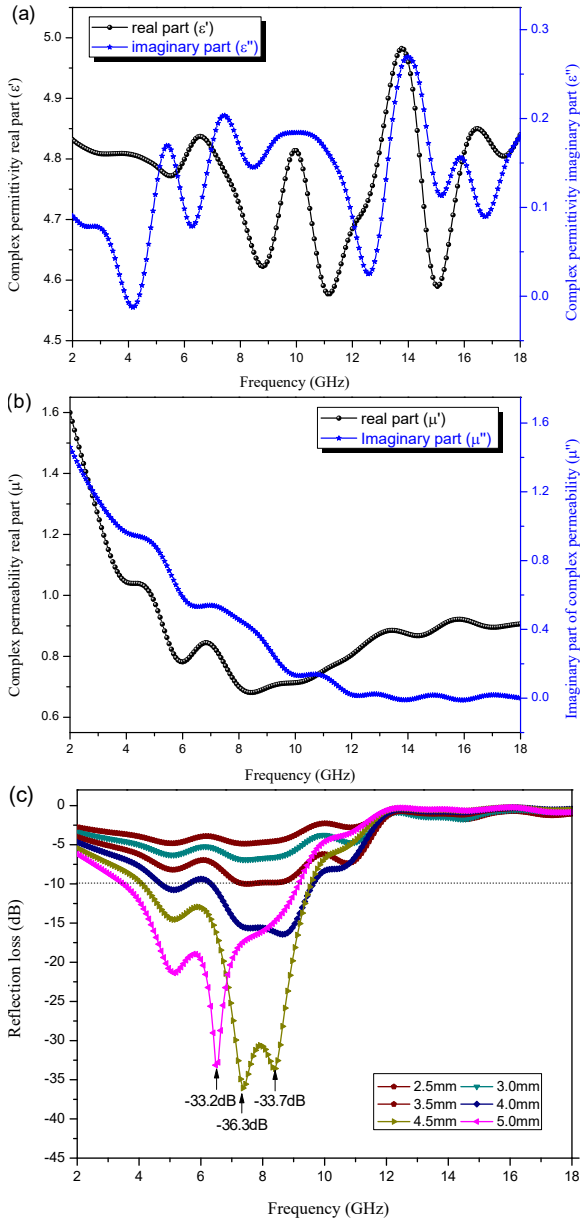

Fig. 7 Electromagnetic parameters and wave absorbing properties of NZCFO: (a) the real part (ε′) and imaginary part (ε″); (b) the real part (μ′) and imaginary part (μ″); and (c) the reflection loss curve with frequency.

of obvious miscellaneous peaks in the diffraction patterns after 4 h at 600–800 °C in air indicated that the samples had good purity. Conversely, there were some clutter peaks after 4 h at 900 °C in air. Based on these data, the pure phase could be synthesized below 900 °C. Moreover, the XRD patterns established that the product synthesized from auto-combustion was a single phase of NZCFO. Subsequent heat treatment of the product caused the diffraction characteristic peak to grow sharper,

which indicated improvement of crystallinity.

The average grain size of the sample could be calculated from the half height and width of the (311) crystal surface and the location of the strongest diffraction peak. The calculation was performed via Debye Scherrer's formula [32]:

$$D = \frac{k\lambda}{\beta \cos\theta} \tag{5}$$

Here, D is the crystal grain size, 0.89 is Scherrer's constant, $\lambda = 1.5406$ Å is the wavelength of the X-ray Cu K_α source, β is the width at half-maximum of the diffraction peaks, and θ is the diffraction angle. Calcinations at 600–800 °C for 4 h caused the grain size of the samples to first decrease from 19.1 ± 0.3 nm to 18.8 ± 0.3 nm, and then increase to 22.3 ± 0.4 nm. These results correspond to the recrystallization of the auto-combusted grains during the heat treatment, which largely reduces grain defects and improves magnetic properties.

Fig. 4 depicted SEM images of the xerogel and post auto-combustion samples. The morphology of the xerogel, as shown in Fig. 4a, was characterized by agglomerated colloids and sparse pores on the surface. As suggested by the TG-DSC analysis, the pores were likely channels formed by the release of steam from the colloid during the 120 °C drying process. Fig. 4b showed the morphology the xerogel after ignition and auto-combustion. The morphologies, when combined with TG-DSC, XRD, and FT-IR analyses, indicated that the nitrate and CA components in the xerogels underwent melting and thermal decomposition during auto-combustion, and that the release of formed gas was responsible for the unique morphology inside the xerogels. The sample depicted in Fig. 4b was calcinated at 600 °C for 4 h, and its detailed morphology is presented in Fig. 4cd. In Fig. 4c, many thin-walled cavities were visible. Visible in the higher-resolution Fig. 4d were not only these cavities, but also many micropores lining the cavity walls. Comparison among Fig. 4b, Fig. 4c, and Fig. 4d, combined with the change of grain size indicated by XRD analysis (Table 2), led us to believe that the recrystallization of ferrite grains after high-temperature calcination causes the formation of a large number of micropores on the cavity walls. These cavities and micropores serve to greatly reduce the bulk density of the sample.

In order to obtain an area on the surface of sample in Fig. 4e and quantitatively determine the elements by EDS(Energy Dispersive Spectrometer), the target element content (Atomic %) of the sample determined by ZAF modification method was Ni:Zn:Cu:Fe ≈ 5.52:2.51:2.17:18.32, close to the preset metal element ratio of $Ni_{0.55}Zn_{0.25}Cu_{0.20}Fe_2O_4$ (Fig. 4f) [33].

The abundance of holes, visible in SEM images of the cross sectioned sample, and cavity walls (Fig. 4b-d) contribute to its porous structure which may help to reduce its bulk density. At room temperature, measured by the Pycnometer method, the bulk density of the powder was about 2.52 g/cm^3 (Table 1), which was about 1/2 of the general ferrite (5.8 g/cm^3) and close to the hollow ferrite (2.3–4.3 g/cm^3) [12–14].

The powder density, ρ, in Table 1 was calculated by the Pycnometer method. Firstly, we weighed the sample powder with mass of m_1, then poured it into a 5 ml volumetric flask. The flask was filled with alcohol, and then weighed the total mass of m_3. The mixture of alcohol and powder in the flask was replaced with alcohol and weighed to obtain a new mass of m_2. The density of alcohol at room temperature was $\rho_0 = 0.7808$ g/cm^3, and the density of powder was obtained by Eq. (6) [34]:

$$\rho = \frac{m_1}{m_1 + m_2 - m_3} \times \rho_0 \tag{6}$$

In order to characterize the pores and low bulk density formed in the NZCFO samples, the samples were vacuum treated at 150 °C for 10 h to remove moisture, and then the N_2 adsorption-desorption isotherms of the samples were measured by a multi-purpose adsorption instrument. The specific surface area and the pore volume were calculated by Barrett-Emmett-Telleller (BET) and Barrett-Joyner-Halenda (BJH) methods, respectively, and the results are shown in Fig. 5ab.

The N_2 adsorption-desorption isotherm curves shown in Fig. 5a indicated that in the low pressure section, the amount of adsorbed N_2 gradually increased across the P/P_0 range of 0.1 to 0.95, although the adsorption curve became very steep and the adsorption capacity increased rapidly for P/P_0 between 0.95 and 1.0. The change to the adsorption curve indicated that the sample had characteristics of a class IV curve [35]. The desorption branch was located above the adsorption branch, and both tended to be parallel in the vicinity of saturated vapor pressure when P/P_0 was between 0.95 and 1.0, forming a hysteresis loop with H3 characteristics [36]. Analyses of the sample morphology and the BJH aperture algorithm using SEM led us to believe that the grains in the NZCFO powder were loose and accumulate into micropores of pore size about 2 nm and mesopores with multi-layered

sheets and of pore size 30 to 100 nm (Fig. 5b). The BET surface Area was 6.68 m^2/g, the BJH adsorption cumulative surface area of pores of 1.70 nm to 300.00 nm in width was 5.00 m^2/g, and the BJH desorption cumulative surface area of pores was 7.40 m^2/g. These features can be attributed to the following: (1) rapid oxidation of the xerogel during the auto-combustion redox process caused rapid release of the gas, which led to the formation of a large number of pore channels; (2) oxidation and elimination of the organic matter in the xerogel caused a reduction of volume and the formation of numerous voids between the grains, which promoted loose packing of grains and contributed to the formation of pores. These pores were beneficial for improving microwave absorption performance and decrease of ferrite body density.

The magnetic properties of the NZCFO nanopowders were studied by VSM magnetometer. The observed hysteresis loop (M–H) curve is shown in Fig. 6. The relative magnetic properties, including saturation magnetization (M_s), coercive force (H_c), and remanent magnetization (M_r) are shown in Table 2.

As shown in Fig. 6 and Table 2, the NZCFO samples prepared by the sol-gel auto-combustion method displayed clear hysteresis behavior, and the M_s, M_r, and H_c of NZCFO-600 were 61.49 emu/g, 13.38 emu/g, and 50.79 Gauss, respectively. The soft magnetic properties were superior to those prepared using the sol-gel method as reported by Gao [37] (M_s = 36 emu/g and H_c = 167 Gauss). With increasing temperature, the M_s of NZCFO gradually increased, while the M_r, H_c, and M_r/M_s first increased and then decreased. Meanwhile, the NZCFO grain size first decreased and then increased gradually, which could be attributed to recrystallization of the sample. The latter phenotype could be attributed to improved sample crystallinity, increased grain size, and decreased number of spin suspension bonds on the surface, which led to increase net spin moment and M_s. When the size exceeded the critical grain size, the domain wall formed gradually as the coercive force decreased [33, 38]. As the grain size grew, so did the M_s, while the M_r, H_c, and M_r/M_s decreased. The NZCFO-800 had the minimum remanence ratio and a narrow hysteresis loop, showing that a soft magnetism, a high remanence ratio, and a small coercive force could improve magnetic and electrical coupling, making it more advantageous in high frequency soft magnetic medium application [39].

The electromagnetic properties of the NZCFO samples were tested by a Vector Network Analyzer. The results are shown in Fig. 7a-c. The dielectric properties were expressed by complex permittivity. The real part was the storage capacity of electric energy, and the imaginary part was the consumption capacity of electric energy [40, 41]. Magnetic properties could be expressed as complex permeability, real part as magnetic energy storage capacity, and imaginary part as magnetic energy consumption capacity [40, 42].

Fig. 7a depicted a diagram of the NZCFO dielectric constant versus frequency. The value of the real component was much higher than that of the imaginary component, indicating that the electric energy storage capacity exceeded the consumption capacity on the dielectric parameters of the sample. Fig. 7b showed the NZCFO permeability versus frequency, wherein the real and imaginary components of the permeability were roughly equivalent, and the permeability values exceeded those reported by Gao [37]. Fig. 7c was the reflection spectrum of the NZCFO across the 2–18 GHz microwave range. The extrema value of −36.3 dB occurred when the film thickness was 4.5 mm, with the peak appearing near 8.0 GHz and the absorption peak band close to 2 GHz. The microwave absorption performance of the film was better than that of diatomite/Ni-Zn ferrite [37].

The electromagnetic properties of spinel ferrite mainly depended on the distribution of metal ions in the crystal structure and the spatial structure of grains. In spinel ferrite, the oxygen ions occupied a cubic close-packed structure, while the metal ions were distributed in the gaps between oxygen ions, as described generally by the following Formula (7):

$$(Me_{\delta}^{2+}Fe_{1-\delta}^{3+})[Me_{1-\delta}^{2+}Fe_{1+\delta}^{3+}]O_4 \qquad (7)$$

The ions in ( ) occupied position A (tetrahedral gap), and the ions in [ ] occupied position B (octahedral gap). In NZCFO, the order of the proclivities of metal ions to occupy position A was $Zn^{2+} > Fe^{3+} > Cu^{2+} > Ni^{2+}$, favoring a cation distribution of $(Zn_{0.25}^{2+}Fe_{0.5}^{3+})[Ni_{0.55}^{2+}Cu_{0.20}^{2+}Fe_{1.5}^{3+}]O_4$ and, therefore, the formation of spinel ferrite [43]. Addition of Zn^{2+} increased the tendency of metal ions to occupy the A-site, and some Fe^{3+} occupying A-site enter the B-site. As the magnetic moment of was about 5 μB, the magnetic moment of Cu^{2+} was about 2 μB, which exceeded that of the non-magnetic Zn^{2+} ion. Displacement of the A-site Zn^{2+} ions by Cu^{2+} ions reduced the net magnetic moment of the B position and the magnetic loss and weakened the absorbing

performance. However, the diffusion of some Cu^{2+} ions to the vacancy of the tetrahedron gap could drive these ions to the B-site and, thereby, increased the net magnetic moment of the B position. This served to enhance the super-exchange effect with the A position magnetic moment, so as to improve the saturation magnetization and permeability of the material, increase its electromagnetic loss, and improve its absorbing performance. Therefore, doping within the NZCFO imbued the material with good microwave absorption performance. On the other hand, the hollow structure was not conducive to the formation of large magnetic domains, which hindered the transmission of magnetism and made the permeability of the sample slightly smaller than that of the diatomite/Ni-Zn ferrite.

CONCLUSION

Porous low-density $Ni_{0.55}Zn_{0.25}Cu_{0.20}Fe_2O_4$ (NZCFO) was prepared via a sol-gel auto-combustion method with controlled temperature and pH values. High purity NZCFO powder, with porous cavity structure, was prepared by calcinating the auto-combustion products of xerogels in air at 600–800 °C for 4 h. The density of the resulting powder is only 2.52 g/cm^3, which was about 1/2 of the general ferrite and close to the hollow ferrite. Absorption tests showed that the NZCFO had good dielectric properties and low reflectivity down to −36.3 dB. Therefore, we developed a novel, efficient microwave absorbing agent with low-density and good absorbing properties.

Acknowledgements: This study was supported by the National Natural Science Foundation of China (21361007).

REFERENCES

1. An YL, Li J, Yuan X, Zheng ZH, Zhang XM (2014) Preparation and electromagnetism property of activated carbon load Ni-Zn ferrite. *Funct Mater* **45**, 28–31.
2. Pransisco PK, Shafie A, Guan BH (2014) Effect of calcination temperature on microstructure and magnetic properties of $Ni_{0.5}Zn_{0.25}Cu_{0.25}Fe_2O_4$ nanoparticles synthesized by sol-gel method. *AIP Conf Proc* **1621**, 619–624.
3. Wakiya N, Muraoka K, Kadowaki T, Kiguchi T, Mizutani N, Suzuki H, Shinozaki K (2007) Preparation of ferromagnetic zinc-ferrite thin film by pulsed laserdeposition in the magnetic field. *J Magn Magn Mater* **310**, 2546–2548.
4. Corral-Flores V, Bueno-Baqués D, Paraguay-Delgado F, Botez CE, Ibarra-Gómez R, Ziolo R (2007) Magnetic properties of nickel-zinc ferrite nanoparticles synthesized by coprecipitation. *Phys Stat Sol(a)* **204**, 1742–1745.
5. Yu QS, Su YC, Tursun R, Zhang J (2019) Synthesis and characterization of low density porous nickel zinc ferrites. *RSC Adv* **9**, 13173–13181.
6. Wushuer M, Xiaerding F, Mamat M, Xu M, Mijiti A, Aihaiti L (2020) Influence of Mn doping on structural, optical, and magnetic properties of $BiFeO_3$ films fabricated by the sol-gel method. *ScienceAsia* **46**, 330–335.
7. Chen X, Chen Z, Hu D (2011) Synthesis technology of nickel-zinc ferrite by hydrothermal method. *Guangdong Chem Ind* **38**, 18–19.
8. Gheisari K, Shahriari S, Rezvanpour A, Javadpour S (2013) Structure and magnetic properties of nanocrystalline $Ni_{0.64}Zn_{0.36}Fe_2O_4$ powders prepared by ball milling. *Powder Metall* **56**, 216–220.
9. Verma A, Goel TC, Mendiratta RG (2000) Frequency variation of initial permeability of Ni-Zn ferrites prepared by the citrate precursor method. *J Magn Magn Mater* **210**, 3274–3278.
10. Misra RDK, Kale A, Srivastava RS, Senkov ON (2013) Synthesis of nanocrystalline nickel and zinc ferrites by microemulsion technique. *Mater Sci Technol* **19**, 826–830.
11. Reddy BR, Sivasankar T, Sivakumar M, Moholkar V (2010) Physical facets of ultrasonic cavitational synthesis of zinc ferrite particles. *Ultrason Sonochem* **17**, 416–426.
12. Wu KH, Ting TH, Liu CI, Yang CC, Hsu JS (2008) Electromagnetic and microwave absorbing properties of $Ni_{0.5}Zn_{0.5}Fe_2O_4$ bamboo charcoal core-shell nanocomposites. *Compos Sci Technol* **68**, 132–139.
13. Gu YY, Peng S, Qin Z, Zhuang SX (2007) Preparation of micropore nickel-zinc ferrite nanosized particle by hydrothermal template process. *J Magn Mater Devices* **38**, 37–39.
14. Cui SP, Wang N, Guo HX, Ma XY (2016) Synthesis and electromagnetic properties of nickel zinc ferrite coated on surface of diatomite. *J Chin Ceram Soc* **44**, 1509–1514.
15. Zhang YQ, Zhang X (2009) Microwave absorbing property and modification of ferrite-encapsulated cenosphere powders. *J Inorg Mater* **24**, 732–736.
16. Yue ZX, Zhou J, Zhang HG, Gui ZL, Li LT (1999) Auto-combustion behavior of nitrate-citrate gels and synthesis of ferrite nano-particles. *J Chin Ceram Soc* **27**, 466–470.
17. Yue ZX, Guo WY, Zhou J, Gui ZL, Li LT (2004) Synthesis of nano-crystilline ferrites by sol-gel combustion process: the influence of pH value of solution. *J Magn Magn Mater* **270**, 216–225.
18. Kavas H, Baykal A, Demir A, Topark MS, Aktas B (2014) $Zn_xCu_{(1-x)}Fe_2O_4$ Nanoferrites by sol-gel auto combustion route: cation distribution and microwave absorption properties. *J Inorg Organomet*

Polym Mater **24**, 963–970.
19. Zhang Y, Lan Z, Yu Z (2006) Synthesis of Ni-Zn ferrite nanoparticles by sol-gel method. *Mater Rep* **5**, 49–51.
20. Choy JH, Yoo JS (1992) Optimization of precursor fiber formation conditions from the Y-Ba-Cu-citric acid-H_2O sol. *Mater Lett* **13**, 232–240.
21. Chen ZS, Xiao SX, Xu JP, Huang HQ (2017) Calculation on optimal pH range of the precursor solution for preparing $Y_2Ti_2O_7$ nanocrystals by citric acid sol-gel technique. *J East China Univ Technol* **40**, 185–190.
22. Cao X, Zhang Y, Cao WG, Zhang YL, Peng D, Xue CL, Tan YX (2018) Influences of mass effect and thermal history on thermal decomposition of ammonium nitrate. *Acta Armamentarii* **39**, 2153–20158.
23. Qi XG, Wang XG, Xia BR (2005) Effect of additives on crystal transition of anti-explosive ammonium nitrate using DSC curves. *Explosive Mater* **34**, 1–3.
24. Zhou S, Xu YB, Wang CH, Tian ZF (2011) Pyrolytic behavior of citric acid. *Tob Chem* **9**, 45–49.
25. Chakrabarti N, Maiti HS (1997) Chemical synthesis of PZT powder by auto-combustion of citrate-nitrate gel. *Mater Lett* **30**, 169–173.
26. Qi XW, Zhou J, Yue ZX, Gui ZL, Li LT (2002) Auto-combustion synthesis of nano-crystalline $LaFeO_3$. *Mater Chem Phys* **78**, 25–29.
27. Moussas PA, Zouboulis AI (2009) A new inorganic-organic composite coagulant, consisting of polyferric sulphate (PFS) and polyacry lamide (PAA). *Water Res* **43**, 3511–3524.
28. Zhu GC, Zheng HL, Zhang Z, Tshukudu T, Zhang P (2011) Characterization and coagulation-flocculation behavior of polymeric aluminum ferric sulfate (PAFS). *Chem Eng J* **178**, 50–59.
29. Wu YH, Li WQ, Shen XM (2003) *Organic Chemistry*, Univ Sci Technol China Press, Hefei, China.
30. Selvan RK, Krishnan V, Augustin CO, Bertagnolli H, Gedanken A (2008) Investigations on the structural, morphological, electrical, and magnetic properties of $CuFe_2O_4$-NiO nanocomposites. *A Chem Mater* **20**, 429–439.
31. Varshosaz J, Sadeghi-aliabadi H, Ghasemi S, Behdadfar B (2013) Use of magnetic folate-dextran-retinoic acid micelles for dual targeting of doxorubicin in breast cancer, *BioMed Res Int* **2013**, ID 680712.
32. Ali I, Islam MU, Awan MS, Ahmad M, Iqbal M (2013) Structural and magnetic properties of nano-structured Eu^{3+} substituted M-type hexaferrites synthesized by sol-gel auto-combustion technique. *J Supercond Novel Magn* **26**, 3315–3323.
33. Jalalian M, Mirkazemi SM, Alamolhoda S (2016) Phase constituents and magnetic properties of the $CoFe_2O_4$ nanoparticles prepared by polyvinylpyrrolidone (PVP)-assisted hydrothermal route. *Appl Phys A* **122**, 835–835.
34. Ni CJ (1991) Density measurement by Pycnometer method. *J Anshan Normal Univ* **3**, 51–52.
35. Brunauer S, Deming LS, Deming WE, Teller E (1940) On a theory of the van der Waals adsorption of gases. *J Am Chem Soc* **62**, 1723–1732.
36. Vafaeezadeh M, Fattahi A (2014) A study on the catalytic activity and theoretical modeling of a novel dual acidic mesoporous silica. *RSC Adv* **4**, 16647–16654.
37. Gao JP, Liu XY, Lu XW, Li XY (2012) Complexing sol-gel method synthesis and characterization of nanocrystalline $Ni_{0.5}Zn_{0.5}Fe_2O_4$ ferrite. *Chin J Inorg Chem* **28**, 1200–1204.
38. Qu YQ, Yang HB, Yang N, Fan YZ, Zhu HY, Zou GT (2006) The effect of reaction temperature on the particle size, structure and magnetic properties of coprecipitated $CoFe_2O_4$ nanoparticles. *Mater Lett* **60**, 3550–3552.
39. Zhao G, Shang YB, Li Q, Zhao LM (2012) Applications of soft magnetic materials in new energy, energy-saving and environment protecting fields. *J Magn Mater Devices* **43**, 1–8.
40. Sun GB, Dong BX, Cao MH, Wei BQ, Hu CW (2011) Hierarchical dendrite-like magneric materials of Fe_3O_4, γ-Fe_2O_3 , and Fe with high perfeormance of microwave absorption. *Chem Mater* **23**, 1587–1593.
41. Zhao B, Shao G, Fan BB, Zhao WY, Chen YQ, Zhang R (2015) Facile synthesis of crumpled ZnS net-wrapped Ni walnut spheres with enhanced microwave absorption properties. *RSC Adv* **5**, 9806–9814.
42. Wang DW, Wang QH, Wang TM (2011) Controlled synthesis of mesoporous hematite nanostructures and their application as electrochemical capacitor electrodes. *Nanotech* **22**, ID 135604.
43. Ma ZJ, Mang CY, Wang JC, Weng XY, Si LW, Guan ZH (2017) Influence of doping with metal ions Co^{2+}, Mn^{2+} and Cu^{2+} on absorbability of nano Ni-Zn ferrite. *Chin J Mater Res* **31**, 909–917.